

---

Review Paper

---

# Backflow Vortex Cavitation and Its Effects on Cavitation Instabilities

Kazuyoshi Yamamoto<sup>1</sup>, Yoshinobu Tsujimoto<sup>2</sup>

<sup>1</sup>Center for Research and Investigation of Advanced Science and Technology,  
Japan Advanced Institute of Science and Technology  
Nomi, Ishikawa, 923-1292, Japan, kazuyosi@jaist.ac.jp

<sup>2</sup>Engineering Science, Osaka University  
Toyonaka, Osaka, 560-8531, Japan, tsujimoto@me.es.osaka-u.ac.jp

## Abstract

Cavitation instabilities in turbo-machinery such as cavitation surge and rotating cavitation are usually explained by the quasi-steady characteristics of cavitation, mass flow gain factor and cavitation compliance. However, there are certain cases when it is required to take account of unsteady characteristics. As an example of such cases, cavitation surge in industrial centrifugal pump caused by backflow vortex cavitation is presented and the importance of the phase delay of backflow vortex cavitation is clarified. First, fundamental characteristics of backflow vortex structure is shown followed by detailed discussions on the energy transfer under cavitation surge in the centrifugal pump. Then, the dynamics of backflow is discussed to explain a large phase lag observed in the experiments with the centrifugal pump.

**Keywords:** Cavitation, Instability, Backflow, Cavitation Surge, Inducer, Centrifugal pump, Vortex

## 1. Backflow Vortex Cavitation

Industrial pumps are usually required to operate in a wide range of flow rate with cavitation. In such cases, a system instability caused by cavitation may occur. This is called cavitation surge. Under low flow rates, a backflow occurs at the outer part of pump inlet due to excessive pressure difference across the blades near the leading edge. The backflow has a high tangential velocity due to the angular momentum imparted by the blades. The shear layer between the swirling backflow and straight main flow rolls up and forms a backflow vortex structure as shown in Fig.1. Backflow vortex cavitation occurs at the vortex core, as shown in Fig.2, if the pressure there becomes lower than the vapor pressure due to the centrifugal force on the vortical motion and the increase of the main flow velocity caused by the displacement effect of the backflow.

For high speed turbo-pumps such as for rocket engines, an axial stage with high solidity is often attached at the inlet of centrifugal main pump, to improve cavitation performance. This axial stage is called “inducer”. Since inducers are usually operated under cavitation, they are designed with a certain incidence angle to secure that the cavitation occurs only on the suction surface to prevent pre-mature head breakdown caused by the cavitation on the pressure surface. From this reason, inducers are operated with certain backflow even at the design point. So, we need to understand fundamental characteristics the backflow at the inlet.

### 1.1 Structure of Backflow Vortices

To show the fundamental characteristics of backflow vortex structure, we consider an inducer as shown in Fig.3 with the specifications given in Table 1, which is analogous to the liquid oxygen turbopump inducer for HII rocket. The picture in Fig.2 was taken at the design flow coefficient of  $\phi_d=0.078$  and the cavitation number  $\sigma=0.050$  at the rotational speed of  $N=3,000\text{rpm}$ . Figure 4 shows the profile of vortex filaments projected to meridional plane, measured by using a laser displacement sensor [1]. The upstream end of the vortex is attached to the pipe wall and the downstream end to the blade surface. This vortex structure moves in the direction of impeller rotation but with much smaller angular velocity than the impeller. Figure 4 shows that the vortex filaments extend more upstream as the flow coefficient is decreased. The radial location of the filaments moves inwards as we decrease the flow coefficient. The scatter of the data points is not caused by measurement errors but indicates the unsteady nature of the filaments.

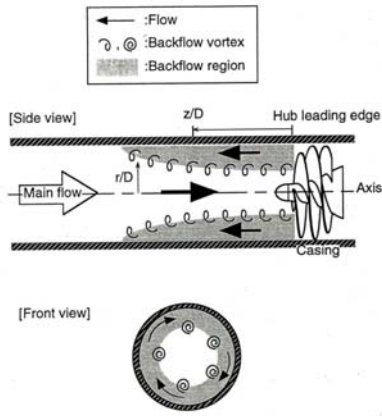


**Fig. 1** Backflow vortex structure at the boundary between swirling backflow and axial main flow

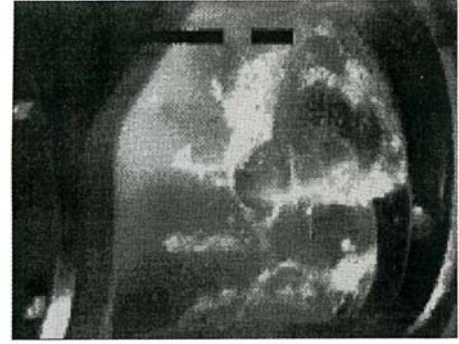


**Fig. 2** Picture of backflow vortex cavitation at the inlet of an inducer ( $\phi = \phi_d = 0.078$ ,  $\sigma = 0.050$ ).

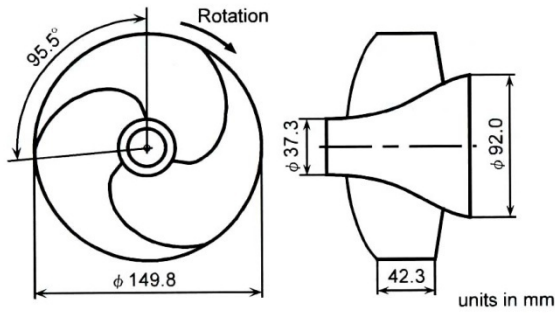


**Fig. 3** Geometry of test inducer

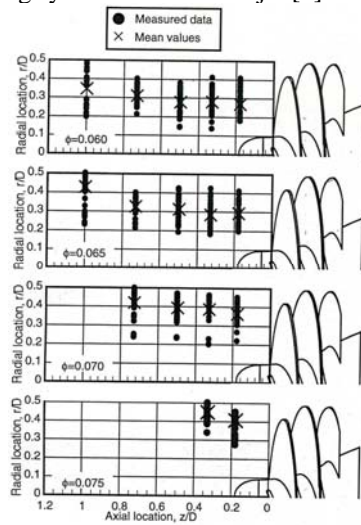
**Table 1** Specification of the inducer

Number of blades	3
Tip diameter $D_t$ (m)	0.1498
Inlet tip blade angle (deg)	7.5
Outlet tip blade angle (deg)	9.0
Hub / tip ratio at inlet	0.25
Hub / tip ratio at outlet	0.51
Solidity at tip	1.91
Design flow coefficient $\phi_d$	0.078
Tip clearance (m)	$0.5 \times 10^{-3}$

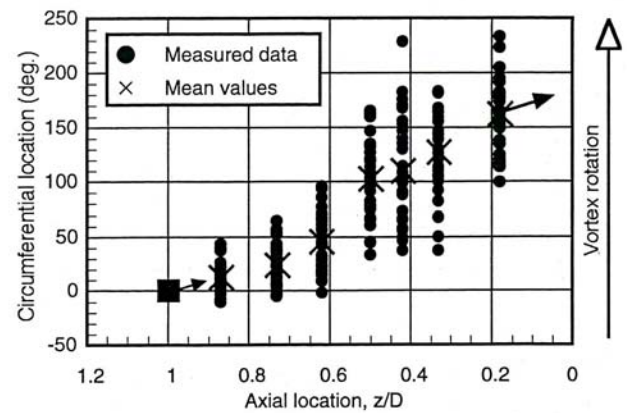
Figure 5 shows the profile of the vortex filaments projected to the axial-circumferential plane. Vortex filaments are skewed in the direction such that the upstream end retards. In the figure, vorticity vectors of mean velocity field at the radial location with maximum shear are shown. Vortex filaments are nearly parallel with these vectors. Figure 6 shows the angular velocity of the vortex structure normalized by the angular velocity of the impeller. The maximum fluid velocity is also shown. The vortex structure rotates with the velocity about a half of the maximum fluid velocity and 10-20% of the impeller speed.

Figure 7 shows the number of vortex filaments. The number of vortices is larger at larger flow coefficient but it decreases as the flow rate is decreased. Note that the number is as large as 16 at higher flow rate.

All of the observations mentioned above show that the vortex structure appears as the roll up of the shear layer between the swirling backflow and axial main flow. The role of the impeller is just to supply the angular momentum to the backflow and it does not affect the vortex structure. This was confirmed by an experiment in which swirling back flow from the impeller was simulated by a swirling symmetrical hollow jet [2].



**Fig. 4** Profile of backflow vortex filament in meridional plane,  $\sigma = 0.05$



**Fig. 5** Profile of vortex filament in axial-circumferential plane ( $z/D=0$  at hub leading edge,  $\phi=0.06$ ,  $\sigma=0.05$ )

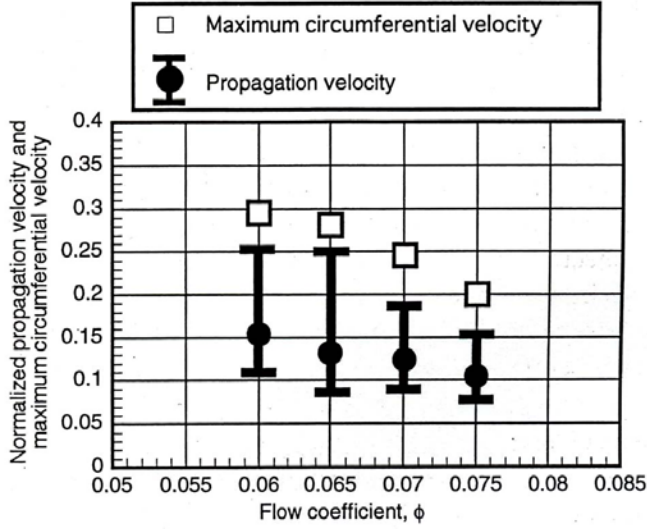


**Fig. 6** Rotational speed of vortex structure, normalized with impeller speed,  $z/D=0.18$ ,  $\sigma=0.05$

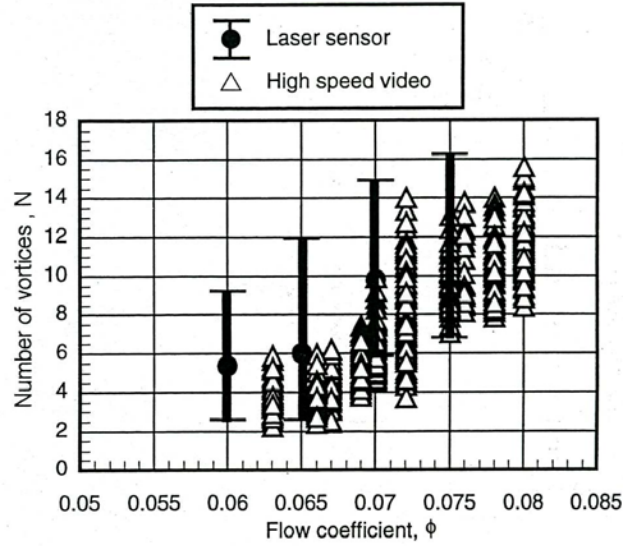


**Fig. 7** Number of vortices,  $z/D=0.18$ ,  $\sigma=0.05$

## 1.2 Stability Analysis of Vortex Structure

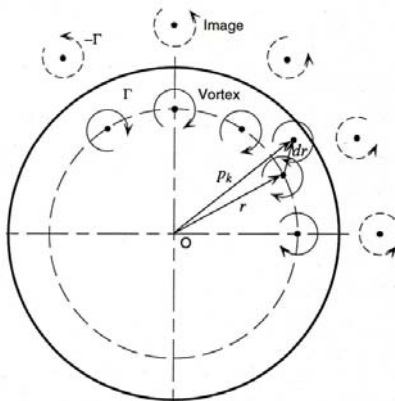
To examine the factor determining the number of vortex filaments, a two-dimensional stability analysis similar to that for Karman vortex street [3] was made. Three dimensional vortex filaments in a circular pipe were modeled by two dimensional vortices in a circular wall as shown in Fig.8 neglecting the skew of the filaments. The boundary condition on the circular wall was satisfied exactly by using image vortices. The assumption that the vortices move on the local induced velocity results in the following equation for the complex displacement  $\delta r$  of the vortices.

$$\frac{d^2 \delta r}{dt^2} = [(A+B)^2 - C^2] \delta r \quad (1)$$

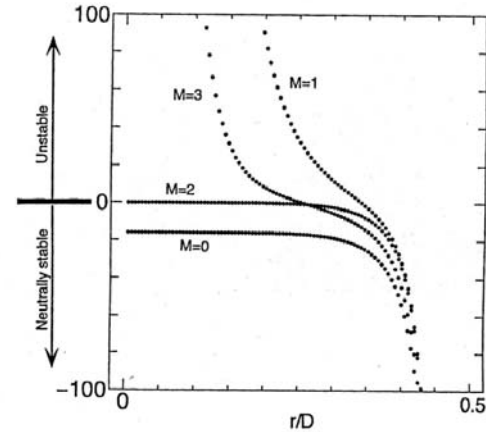
where  $A$ ,  $B$ , and  $C$  are real functions of the radial location of the vortices,  $r$ , the number of vortices,  $N$ , and the mode number  $M$  of the disturbance imposed. The vortex system is unstable when  $[(A+B)^2 - C^2] > 0$  neutrally stable when  $[(A+B)^2 - C^2] < 0$ . So,  $[(A+B)^2 - C^2]$  is herein called stability parameter.

Figure 9 shows the values of stability parameter obtained for the case of four vortices,  $N=4$ . The circumferential disturbance mode number  $M$  is changed from 0 to 3. When the stability parameter is positive, the displacement of the vortices increases exponentially. On the contrary, when the stability parameter is negative, the vortices oscillate around the mean location with a constant amplitude. In Fig.9, the parameter becomes negative for all mode numbers for the radial location  $r/D$  larger than 0.345. Thus, the critical radius above which the vortex structure becomes neutrally stable can be determined as a function of the number of vortices,  $N$ .

Figure 10 shows the critical radius as a function of the number of vortices,  $N$ . The critical radius becomes larger as the number of vortices becomes larger. This means that larger number of vortices can exist quasi-stably if they are located closer to the outer wall. The number of vortices and the radial location evaluated at  $z/D=0.18$  in the inducer test is also shown. All averaged data points are in "unstable" region. However, we should note that the radial location at  $z/D=0.18$  is used for the plot. As shown in Fig.4, the vortex filament gets closer to the pipe wall in the upstream. If we take the averaged value of  $r/D$  at the inducer inlet ( $z/D=0.18$ ) and the location where the vortex attaches the pipe wall, the experimental result (the middle point between experimental data and  $r/D=0.5$ ) agrees remarkably well with the result of the stability analysis. However, it has not been explained why the maximum number of neutrally stable vortices occurs in the experiment.



**Fig. 8** Two-dimensional model for stability analysis



**Fig. 9** Values of stability parameter  $[(A+B)^2 - C^2]$  for  $N=4$

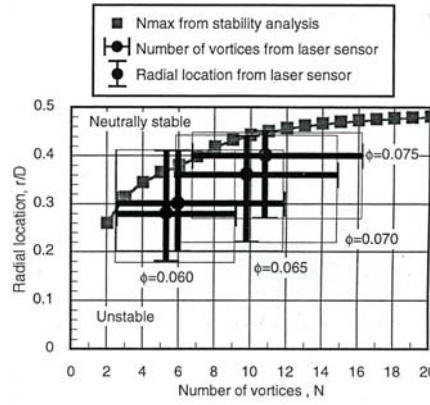


Fig. 10 Critical radius as a function of number of vortices. Experimental data at  $z/D=0.18$ ,  $\sigma=0.05$

## 2. Cavitation Surge in Centrifugal Pump

### 2.1 General Characteristics

Figure 11 shows the specification of the centrifugal pump for the experiments and the cut out drawing. Figure 12 shows the test facility [4]-[6]. The pump has a smooth head-flow rate curve with negative slope from shut-off to the maximum efficiency flow rate  $\phi=0.088$ . The rotational speed was kept to be  $3,000\text{rpm}$ . The volume of the tank is  $2\text{m}^3$  and the pressure level was changed by using a vacuum pump. Magnetic flow meters with the frequency range up to  $20\text{Hz}$  were placed  $17D_1$  upstream and  $20D_2$  downstream from the inlet and outlet of the pump. Pressure measurements were made with resistance type pressure transducers placed at  $13D_1$  upstream and  $2D_2$  downstream from the pump.

Figure 13 shows the suction performance curve obtained with the inlet pipe length  $l_1=2.7\text{m}$  and the outlet pipe length  $l_2=17.4\text{m}$ . Closed symbols show the operating conditions where cavitation surge was observed. Figure 14 shows the onset regions of three types of cavitation surge, as sketched on the right hand side, for the three cases of inlet pipe length shown in the figure, with the outlet pipe length of  $l_2=17.4\text{m}$ . The flow coefficient below which the backflow occurs is shown by  $\phi_c$ . With Type A oscillation, the blade surface cavity oscillation was observed with backflow but without backflow vortex cavitation. The backflow vortex cavitation oscillates with Type B. No backflow was observed with Type C oscillation with oscillating blade surface cavitation. Here, we focus on the Type B oscillation.

Specific Speed	228
Eye Diameter	$\phi 109$
Outlet Diameter	$\phi 218$
Inlet Blade Angle Hub Side	$31^\circ$
Inlet Blade Angle Shroud Side	$18^\circ 15'$
Number of Blade	3

Specific Speed ( $\text{rpm}, \text{m}^3/\text{min}, \text{m}$ )

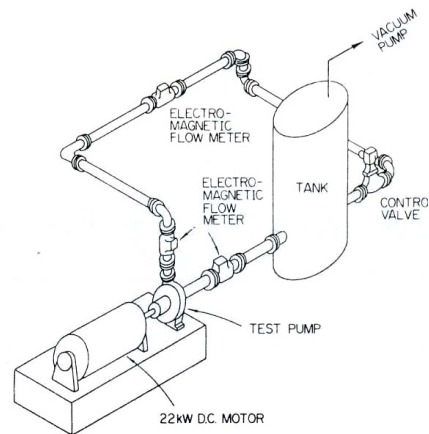
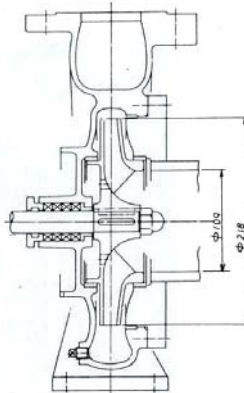


Fig. 11 Specifications and the geometry of centrifugal pump

Fig. 12 Test facility

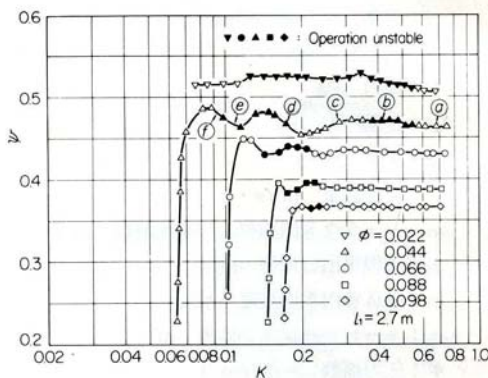


Fig. 13 Suction performance curve

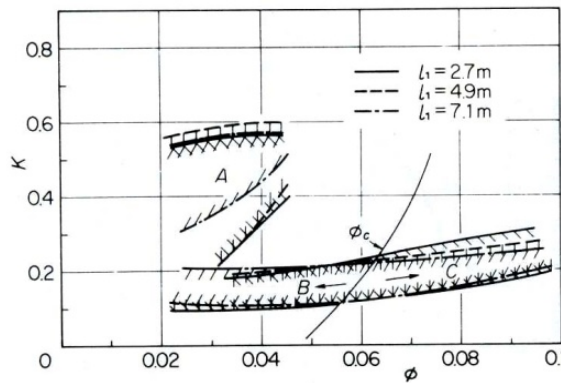
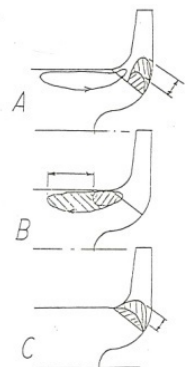
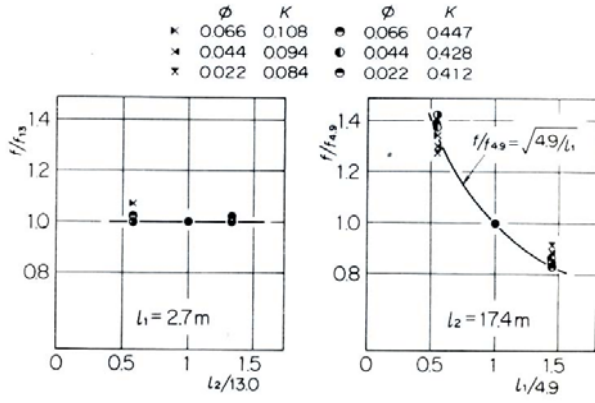


Fig. 14 Ranges of three types of cavitation surge







**Fig. 15** Effects of inlet and outlet pipe lengths on the frequency of cavitation surge

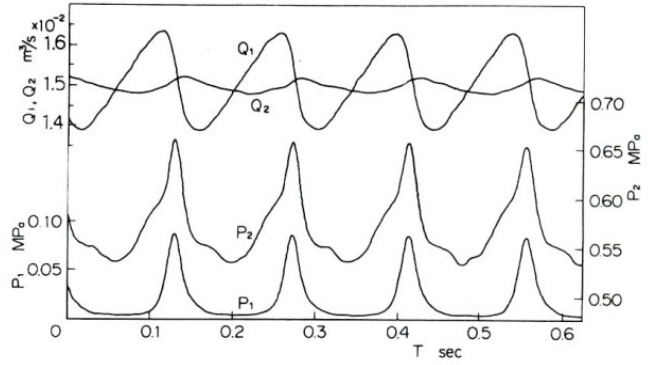


**Fig. 16** Flow rate and pressure fluctuations under Type B cavitation surge, at  $\phi=0.044$  and  $K=0.20$

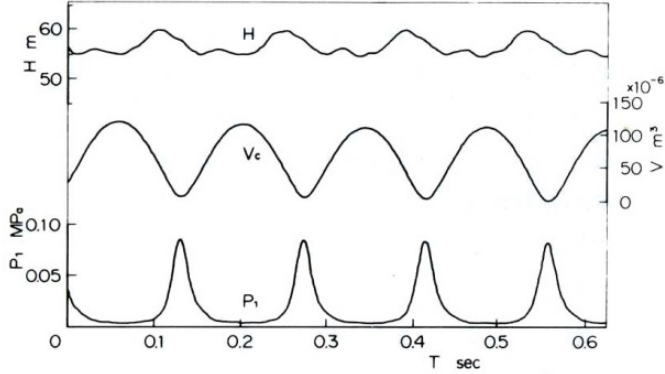


**Fig. 17** Head and cavity volume fluctuations under Type B cavitation surge, at  $\phi=0.044$  and  $K=0.20$

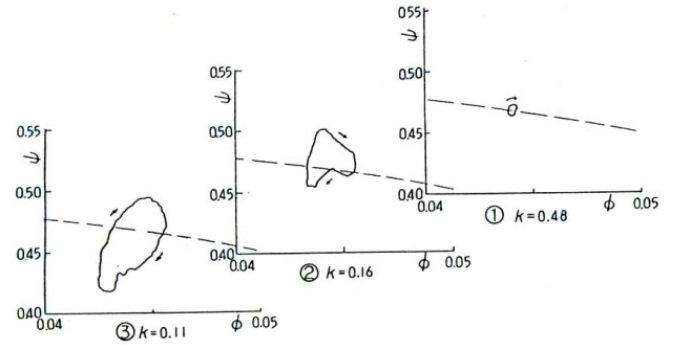


**Fig. 18** Head fluctuation under Type B cavitation surge, at  $\phi=0.044$

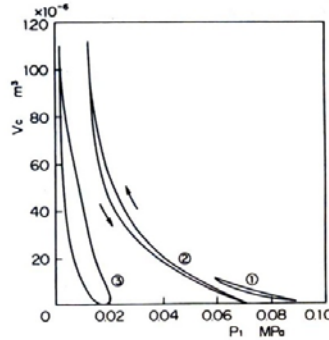


**Fig.19** Cavity volume fluctuation under Type B cavitation surge, with  $\phi=0.044$ , ①  $K=0.48$ , ②  $K=0.16$ , ③  $K=0.11$

Figure 15 shows the effects of inlet and outlet pipe lengths on the frequency. It is shown that the effect of outlet pipe length is negligible while the frequency is scaled with the inverse of the square root of the inlet pipe length, for all three types of oscillation. This shows that the mode of oscillation is such that the inlet flow rate fluctuates with nearly constant outlet flow rate, caused by larger resistance and inductance of the discharge line.

Figure 16 shows the fluctuations of pressure and flow rate for Type B oscillation with the mean flow coefficient of  $\phi=0.044$  and the cavitation number  $K=0.20$ . The downstream flow rate fluctuation is much smaller than the upstream one. This is consistent with the result that the frequency of oscillation is independent on the downstream pipe length.

The cavity volume fluctuation was evaluated from the flow rate fluctuations at the inlet and outlet, and the head fluctuation by compensating the inertia effects of the fluids in the inlet pipes and the pump itself. The results are shown in Fig.17. The pressure peak occurs at the instant when the cavity volume becomes the minimum. The head becomes maximum while the cavity is collapsing, and minimum when the cavity volume becomes the maximum. In Fig.18, the head fluctuation is also shown in the  $\phi$ - $H$  plane for  $\phi=0.044$ . The broken line shows the steady performance. For Type A oscillation at  $K=0.48$ , the amplitude of oscillation is smaller. For Type B oscillations with  $K=0.16$  and  $0.11$ , the amplitude is larger and exhibits a clockwise closed curves. At  $K=0.11$ , the part of the curve with positive slope becomes larger. This can cause the instability as will be discussed shortly. In all cases, the instantaneous operating point moves in clockwise direction. Figure 19 shows the relation between the instantaneous cavity volume and the inlet pressure. In all cases, the data points move in counterclockwise direction. This shows

that the displacement work of cavitation,  $E_{c1} = \int_0^T p_1 dV_c$ , is positive for all the cases.

## 2.2 Discussions on Energy Transfer

Here, we consider the energy balance in the hydraulic system shown in Fig.20 neglecting the effects of viscosity. The energy transferred from the pump, valve, and the tanks should equal the increase of the kinetic energy in the inlet and outlet pipes. This can be expressed as:

$$(P_2Q_2 - P_1Q_1) - (P_3Q_2 - P_0Q_2) + (P_0Q_1 - P_0Q_2) = L_1Q_1\dot{Q}_1 + L_2Q_2\dot{Q}_2 \quad (2)$$

By separating each quantity into averaged and fluctuating (shown by lower case letters) components and considering that the average of the fluctuating component becomes zero, we obtain the following result.

$$(p_2 - p_1)q_2 - p_3q_2 + (q_2 - q_1)p_1 = L_1q_1\dot{q}_1 + L_2q_2\dot{q}_2 \quad (3)$$

The first term shows the energy supplied by the pump,

$$\dot{E}_{p1} = (p_2 - p_1)q_2$$

the second the energy dissipation by the valve,

$$\dot{E}_{v1} = p_3q_2$$

and the third the displacement work of cavitation,

$$\dot{E}_{c1} = (q_2 - q_1)p_1$$

Under steady oscillations, integrated quantities over a period should satisfy the following relation.

$$E_{p1} - E_{v1} + E_{c1} = 0 \quad (4)$$

Figure 21 shows the energy relations for Type B oscillation at  $\phi=0.044$ . We find that the relation (4) is satisfied approximately. At higher cavitation number, the displacement work by cavitation,  $E_{c1}$ , is larger but the contribution of pump work,  $E_{p1}$ , becomes larger at smaller cavitation number.

Figure 22 shows the instantaneous work transfer at  $\phi=0.044$  and  $K=0.16$ . The positive work occurs when the cavity volume starts to increase (①-②) and during the cavity collapse (③-④).

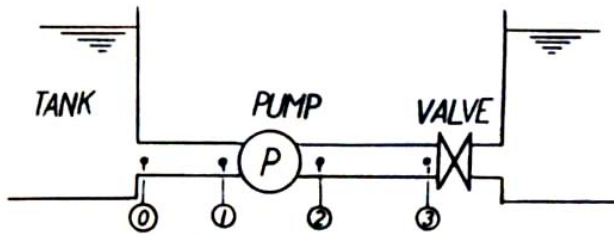


Fig. 20 Hydraulic system

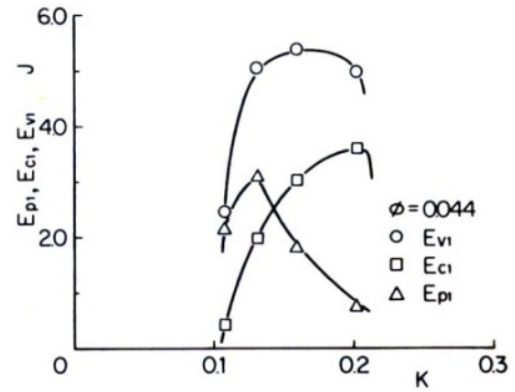


Fig. 21 Energy balance under Type B cavitation surge.

$E_{p1}$ :Energy supplied by pump,  $E_{c1}$ :Displacement work by cavitation,  $E_{v1}$ :Energy dissipated by valve

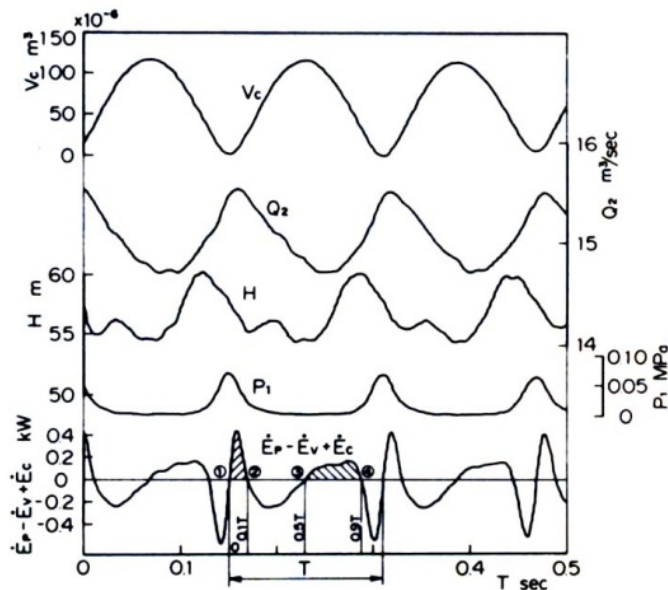


Fig. 22 Instantaneous energy transfer under Type B cavitation surge, at  $\phi=0.044$  and  $K=0.16$

### 2.3 Discussions Based on Mass Flow Gain Factor and Cavitation Compliance

It is well known that cavitation instabilities including cavitation surge and rotating cavitation can be explained by using the quasi-steady characteristics of cavitation, mass flow gain factor and cavitation compliance [7]. These factors were first introduced by Brennen and Acosta [8] to represent the unsteady characteristics of cavitating pumps. The definition of those parameters used here is somewhat different from the original but the physical meanings are the same.

The cavitation compliance is defined as

$$C_p = \partial V_c / \partial P_1 \quad [\text{m}^3/\text{Pa}],$$

and the mass flow gain factor by

$$M_b = \partial V_c / \partial Q_1 \quad [\text{s}],$$

assuming that the steady cavity volume  $V_c$  is a function of the inlet pressure  $P_1$  and the inlet flow rate  $Q_1$ . With these definitions, both  $C_p$  and  $M_b$  will generally have negative values since the cavity volume will decrease if we increase the inlet pressure or the flow rate. If we further assume that the unsteady cavity volume follows quasi-steady relation, we can represent

$$\dot{V}_c = C_p \dot{P}_1 + M_b \dot{Q}_1 \quad (5)$$

The continuity equation across the cavitating pump is,

$$\dot{V}_c = q_2 - q_1 \quad (6)$$

If we represent the resistance and the inertance of the inlet pipe by  $R_1$  and  $L_1$ , the momentum equation applied to the fluid in the inlet pipe results in

$$P_1 = -L_1 \dot{Q}_1 - R_1 q_1 \quad (7)$$

From equations (5)-(7), we obtain

$$-L_1 C_p \ddot{q}_1 + (M_b - R_1 C_p) \dot{q}_1 + q_1 = q_2 \quad (8)$$

For the present case with large downstream resistance and inertance, we can assume  $q_2 \sim 0$ . For this case, negative damping occurs when  $M_b < R_1 C_p$ . Since the value of  $C_p$  is generally negative, instability occurs when the mass flow gain factor has a large negative value. By using the expressions (5) and (7), the displacement work by cavitation can be represented by

$$E_{c1} = \int_0^T P_1 dV_c = \int_0^T (C_p P_1 \dot{P}_1 - M_b L_1 \dot{Q}_1^2) dt \quad (9)$$

where the resistance of the inlet pipe has been neglected. Since the first term is integrated to be zero under steady oscillations, the displacement work becomes positive when the mass flow gain factor has a negative value.

Equation (8) shows also that the frequency of surge can be given by

$$f_0 = 1/(2\pi\sqrt{-L_1 C_p}) \quad (10)$$

which is the resonance frequency of a system composed of the mass of the liquid in the inlet pipe, and the compliance caused by cavitation at the pump inlet.

### 2.4 Evaluation of Mass Flow Gain Factor and Cavitation Compliance

The values of cavitation compliance and mass flow gain factor were evaluated from the resonant frequency. For this purpose, excitation tests were carried out and the resonance frequency was determined from the transfer function between the inlet and outlet mass flow fluctuations. Figure 23 shows the dependence of the resonant frequency on the cavitation number. From this result, the resonant frequency is approximated by

$$f_0 = \lambda K^n / (2\pi\sqrt{L_1}) \quad (11)$$

where  $\lambda$  is a function of flow rate. From equations (10) and (11), we obtain

$$C_p = -1/(\lambda^2 K^{2n}) = \partial V_c / \partial P_1 \quad (12)$$

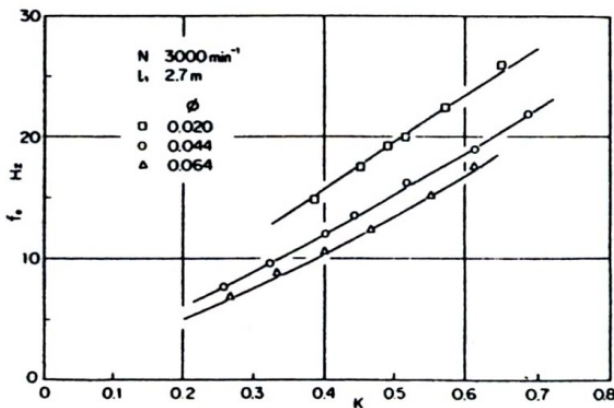


Fig. 23 Effects of cavitation number on resonant frequency

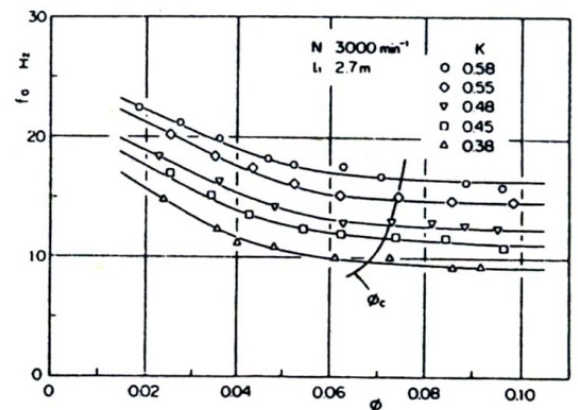


Fig. 24 Effects of flow coefficient on resonant frequency.

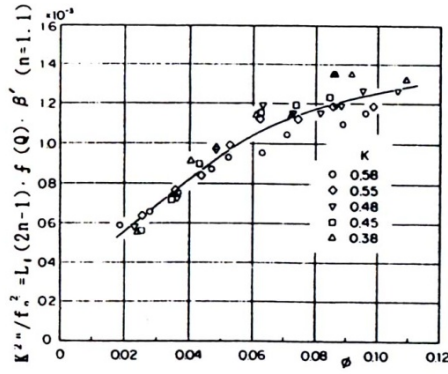


Fig. 25 Quantity of LHS of Eq.(14)

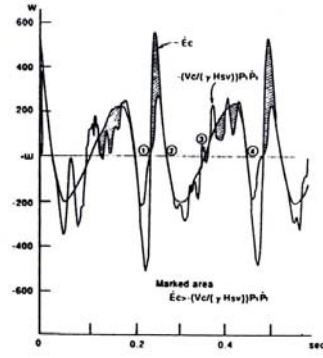


Fig. 26 Components of cavity displacement work  $E_c$ , at  $\phi=0.044$  and  $K=0.16$

By integrating Eq.(12) using  $\beta \equiv \partial K / \partial P_1$ , we obtain

$$V_c = f(Q) / K^{2n-1} \quad (13)$$

where  $f(Q) = 1 / [(2n-1)\lambda^2 \beta]$  is a function of flow rate. By eliminating  $\lambda$  from this expression of  $f(Q)$  and Eq.(11), we obtain

$$K^{2n} / f_0^2 = L_1 (2n-1) f(Q) 4\pi^2 \beta \quad (14)$$

while

$$M_b = \partial V_c / \partial Q_1 = (1 / K^{2n-1}) df(Q) / dQ \quad (15)$$

Figure 24 shows the dependence of the resonant frequency on the flow rate. The frequency increases as the flow rate is decreased. Based on this result, the quantity on the left hand side of Eq.(14) is plotted against the flow coefficient in Fig.25. This shows that  $f(Q)$  is an increasing function of  $Q$  and Eq.(15) shows that  $M_b$  is always positive.

Thus, the stability analysis based on the quasi-steady assumption of cavity volume fluctuation of Eq.(5) failed to explain the instability observed in experiments.

However, the expression of Eq.(5) provides further information about the observed instability. By using Eq.(5), the displacement work of cavitation can be expressed as

$$\dot{E}_c = p_1 \dot{V}_c = C_p p_1 \dot{p}_1 - M_b L_1 \dot{q}_1^2 = -(V_c / \gamma H_{sv}) p_1 \dot{p}_1 - L_1 \{ df(Q) / dQ \} \dot{q}_1^2 / K \quad (16)$$

where  $C_p = -V_c \beta / K = -V_c / \gamma H_{sv}$  has been used.

Figure 26 shows the total displacement work  $\dot{E}_c$  and the first term on the right hand side of Eq.(16), for  $\phi=0.044$  and  $K=0.16$ . The first term does not contribute to the resultant work after integration over a period. The shaded area represents the second term which contributes to the resultant positive displacement work. We find that positive contribution of the second term occurs during the periods ①-② and ③-④ where  $\dot{E}_c$  is positive.

## 2.5 Evaluation of Backflow

In order to evaluate the extent of backflow, the axial velocity  $V_0$  at the center of the inlet pipe was measured near the pump inlet and shown in Fig.27, where  $l_m$  is the distance of the measurement point from the pump inlet. At larger flow coefficients, the axial velocity decreases with the decrease of the flow coefficient. However, at smaller flow coefficients, the axial velocity increases as the flow coefficient is decreased. This is caused by the increase of the displacement effect of backflow at smaller flow rate.

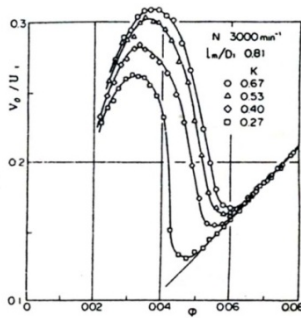


Fig. 27 Velocity at the centre of pump inlet

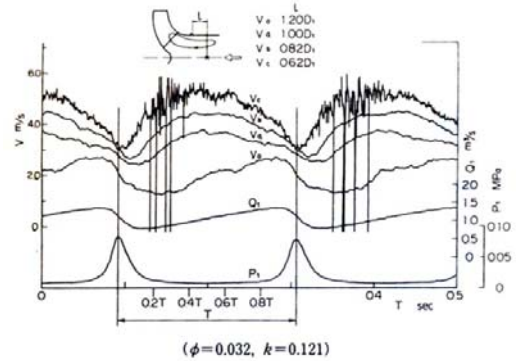
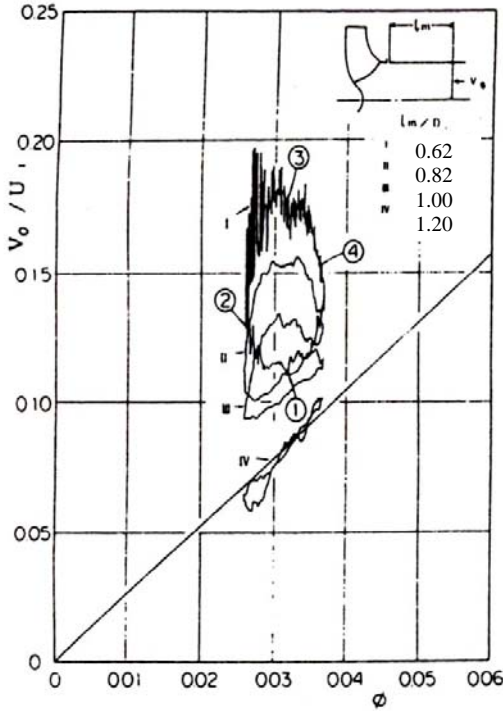


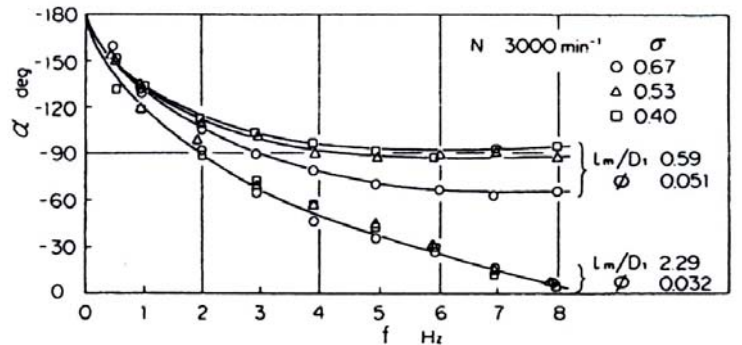
Fig. 28 Velocity fluctuations at the center of pump inlet, under Type B cavitation surge



Figure 28 shows the fluctuation of axial velocity measured at various axial locations under Type B oscillation, at  $\phi=0.032$  and  $K=0.121$ . At far upstream with  $l_m=1.2D_I$ , the velocity fluctuation is nearly in phase with the flow rate fluctuation. As the measurement location approaches the pump inlet, the averaged velocity increases and the time where the maximum velocity occurs is advanced. However, the time with the maximum velocity is somewhat delayed behind the time where the flow rate becomes minimum. This shows that the development of backflow is delayed behind the flow rate fluctuation.



**Fig. 29** Velocity fluctuation at the centre of pump inlet, plotted against instantaneous flow coefficient, for  $\phi=0.044$  and  $K=0.16$



**Fig. 30** Phase angle of inlet velocity fluctuation relative to flow rate fluctuation

Figure 29 shows the plot of axial velocity against the instantaneous flow rate, for  $\phi=0.044$  and  $K=0.16$ , the same as for Fig.26. At the upstream measurement location with  $l_m/D_I=1.2$ , the axial velocity fluctuates in phase with the flow rate. However, at the measurement point with  $l_m/D_I=0.62$ , there are two periods where the velocity is larger with smaller instantaneous flow rate. These periods are denoted by ①-② and ③-④, which correspond to the periods where the displacement work of cavitation becomes positive. This suggests that the increase of the backflow due to the decrease of flow rate is important for the onset of instability. If the backflow increases, the pressure at the inlet will be decreased due to the increase of the axial velocity in the main flow and hence, the cavity volume will be increased. The cavity volume will also increase since the area of the boundary between the swirling backflow and the axial main flow, and the strength of the shear layer corresponding to the strength of backflow are increased. This mechanism is quite natural from quasi-steady considerations but opposed to the results of positive mass flow gain factor evaluated from the measurements of natural frequency. These discrepancies might be explained by considering the unsteady response of backflow to flow rate fluctuation.

## 2.6 Backflow Response to Flow Rate Fluctuation and it's Role in Cavitation Surge at Low Flow Rate

In order to determine the unsteady response of backflow, the phase of the central velocity fluctuation at the inlet,  $V_0$ , was measured under an excitation the hydraulic system in the downstream. Figure 30 shows the phase of the velocity fluctuation  $V_0$ , relative to the upstream flow rate fluctuation. At the frequency of zero, the phase of the central velocity is advanced by 180deg ahead of the flow rate fluctuation. As the frequency is increased, the phase advance is decreased, in other words, the phase delay behind the quasi-steady response is increased. Near the inlet ( $l_m/D_I=0.59$ ), the phase delay approaches 90deg, although larger delay is observed further upstream ( $l_m/D_I=2.29$ ). The larger delay at the upstream is caused by the direct effect of flow rate fluctuation or the time required for the disturbance to propagate upstream from the pump inlet to the axial location of velocity measurement.

If we assume that the cavity volume fluctuation is in phase with the axial velocity fluctuation  $V_0$ , and delays behind the quasi-steady response by  $\pi$ , we can examine the stability by putting  $M_b = M_{b0} \exp(-i(\pi + \alpha))$ ,  $q_2 = 0$  and  $q_1 = q_{10} \exp(i\omega t)$  in Eq.(8). Then the onset condition of cavitation surge can be obtained to be

$$M_{b0} \cos(\pi + \alpha) < R_1 C_p$$

With a negative value of  $M_{b0}$  as expected from quasi-steady consideration, this condition is satisfied when  $\alpha < -90^\circ$  for the case with  $R_1 = 0$ . The results in Fig.30 show that the backflow cavity will excite only lower frequency oscillations than about 4Hz. In Fig.31, this critical frequency  $f_{90}$ , where  $\alpha$  becomes -90deg, is plotted against the cavitation number along with

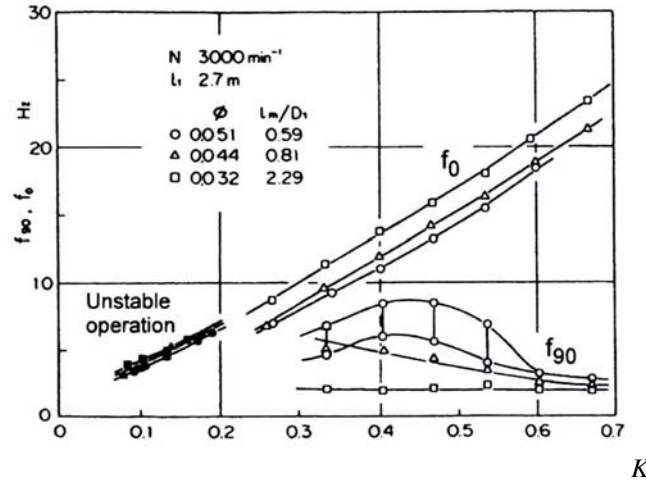


**Fig. 31** Plots of resonant frequency  $f_0$ , critical frequency  $f_{90}$  and the frequency of cavitation surge

resonant frequency  $f_0$  and the frequency of observed cavitation surge. At higher cavitation number, the resonant frequency  $f_0$  is larger than the critical frequency  $f_{90}$  and the system is not destabilized by the backflow vortex cavitation due to the higher phase lag of backflow response. However, as the cavitation number is decreased, the resonant frequency decreases and approaches the critical frequency. Unstable operation is observed in the range of cavitation number where the resonant frequency would be less than the critical frequency.

In summary, it was found that the cavitation surge observed at lower flow rate where backflow occurs is caused by the quasi-steady characteristics of backflow vortex cavitation. When the upstream flow rate is decreased, the main flow velocity is increased due to the increased blockage effect of backflow. This causes the pressure decrease at the inlet. In addition, the pressure in the backflow vortex would be decreased due to the increase of the circulation of the backflow vortex. The axial length of the backflow vortex is also increased. All of these contribute to increase the volume of backflow vortex cavitation with the decrease of the flow rate. The increase of cavity volume affects to decrease the upstream flow rate further, since the downstream flow rate is kept nearly constant due to larger resistance and inertance in the downstream. This positive feed-back is the cause of the cavitation surge observed with the centrifugal pump at lower flow rate. At higher cavitation number, the resonant frequency is higher. At higher frequencies, significant delay of backflow relative to flow rate fluctuation occurs. This delay of backflow prevents the positive feedback and hence the cavitation surge. Thus, the delay of backflow response plays an important role for the stable operation at higher cavitation number and at lower flow rate where backflow vortex cavitation occurs.

### 3. Analysis of Backflow Response

In the last section, it was shown that the backflow vortex cavitation and its response to flow rate fluctuation plays an important role in the cavitation surge of industrial centrifugal pump at reduced flow rate. For inducers, the backflow vortex cavitation occurs even at design flow rate. So, it is very important to understand the dynamic characteristics of backflow vortex cavitation. Although Fig.30 shows certain effect of cavitation on the backflow vortex response, the dynamic characteristics of backflow is not well understood even without cavitation. So, the unsteady characteristics of backflow are treated in this section under non-cavitating condition.

#### 3.1 Method of Analysis and Geometry

Analysis was made for an inducer as shown in Fig.3 and Table 1. Calculations were made by using a commercial code CFX-TASCflow based on RANS with the k- $\epsilon$  turbulence model [9]. For the simulation of the backflow vortex structure, it is required to use a LES code [10] and the present calculation could not simulate the vortex structure. Figure 32 shows the comparisons of the performance and the backflow length with experiments. Although the present code cannot simulate the vortex structure, it can predict the performance and the length of the backflow reasonably.

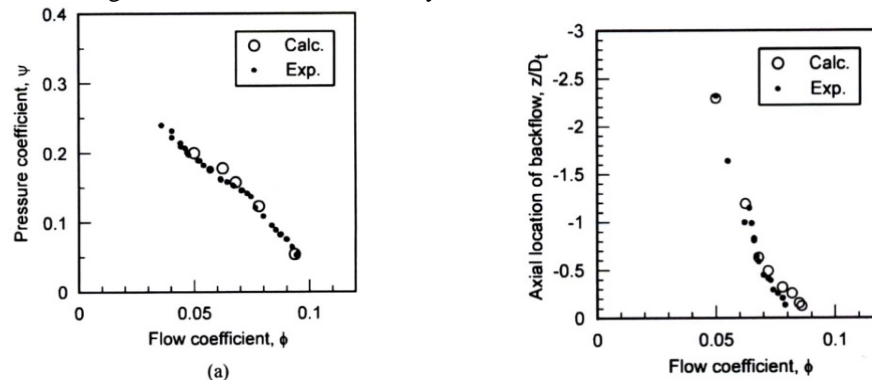


**Fig. 32** Comparison of performance curve and axial length of backflow

### 3.2 Resonse of Backflow to Flow Rate Fluctuations

We consider the flow rate fluctuations expressed by

$$\phi = 0.078 + 0.01\sin(2\pi ft) \quad (17)$$

where 0.078 is the design flow coefficient. The cases with  $f/f_n = 0.0625$ , 0.125 and 0.25 where  $f_n$  is the rotational frequency, are examined. The period of the flow rate fluctuation corresponds to 16, 8, and 4 rotations of the impeller, respectively.

In order to clarify the mechanism of backflow response, we consider the balance of angular momentum in the upstream of the inducer. First, we define the angular momentum in the upstream:

$$AM = \iiint_V \rho r^2 v_\theta dr d\theta dz / (\rho U_t D_t^4) \quad (18)$$

where  $V$  represents the region upstream of a control surface at the blade leading edge at the hub.

The fluctuation of angular momentum is shown in Fig.33 with its quasi-steady values. If we compare the  $AM$  with the length of the backflow shown in Fig. 34, we find that  $AM$  fluctuates in the same phase as the backflow length fluctuation. So, we will use  $AM$  to represent the size of the backflow region. The amplitude of  $AM$  significantly decreases and the phase is delayed as we increase the frequency.

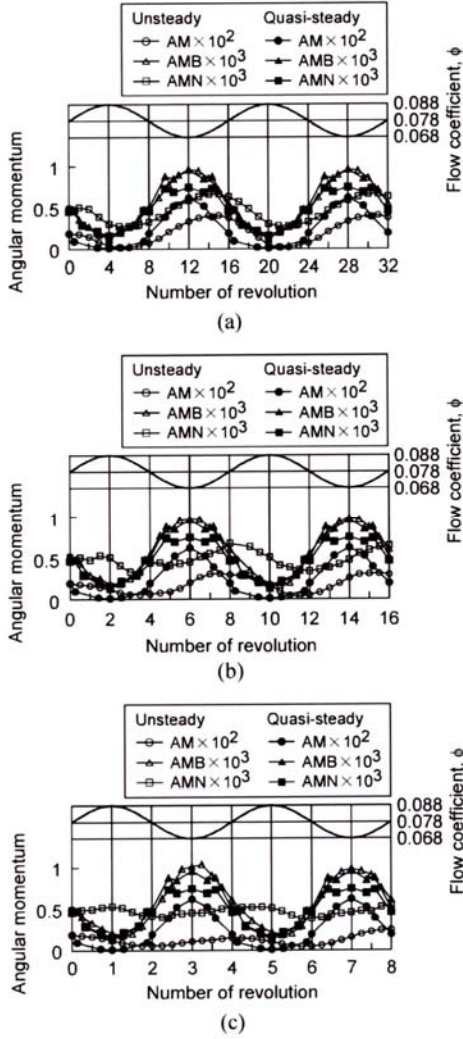


**Fig. 33** Angular momentum fluctuation  
(a)  $f/f_n = 0.0625$ , (b)  $f/f_n = 0.125$ , (c)  $f/f_n = 0.25$

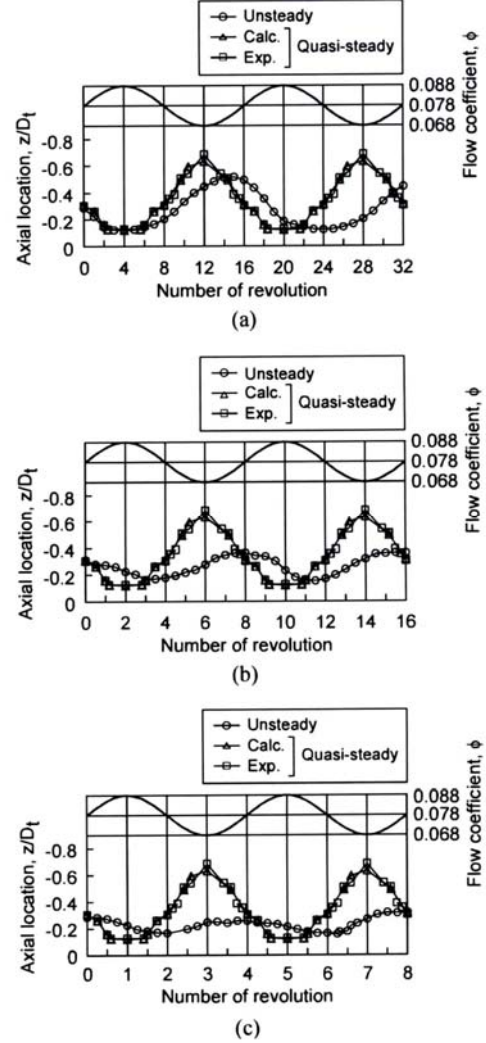


**Fig. 34** Fluctuation of backflow length  
(a)  $f/f_n = 0.0625$ , (b)  $f/f_n = 0.125$ , (c)  $f/f_n = 0.25$

Next, we consider the transport of angular momentum across the control surface. The angular momentum supplied by the backflow ( $v_z < 0$ ),  $AMB$ , and the angular momentum removal by the normal flow ( $v_z > 0$ ),  $AMN$ , are defined as

$$AMB = - \iint_{v_z < 0} \rho r^2 v_\theta v_z dr d\theta / (\rho U_t^2 D_t^3) \quad (19)$$

$$AMN = \iint_{v_z > 0} \rho r^2 v_\theta v_z dr d\theta / (\rho U_t^2 D_t^3) \quad (20)$$

where  $v_z < 0$  and  $v_z > 0$  mean the integration over the region with  $v_z < 0$  and  $v_z > 0$ , respectively.

Figure 33 also shows the fluctuations of  $AMB$  and  $AMN$  with their quasi-steady values. We observe that:

- (1)  $AMB$  has a phase opposite to the flow rate fluctuations;
- (2)  $AMB$  is almost identical to its quasi-steady value;
- (3) Under quasi-steady conditions,  $AMB$  and  $AMN$  agree with each other except when the flow rate is very small. This suggests

that the size of backflow is determined from the balance of  $AMB$  and  $AMN$  for the quasi-steady flow. The unbalance observed at small flow rate should be caused by the skin friction exerted by the pipe wall;

(4) The amplitude of  $AMN$  becomes smaller and the phase delays as we increase the frequency.

If we neglect the effects of shear stress on the boundary of the control volume, the conservation of angular momentum can be represented by

$$d(AM)/dt^* = AMB - AMN \quad (21)$$

where,  $t^* = t/(D/U_t)$  is a non-dimensional time.

Figure 35 examines the dynamic angular momentum balance of Eq.(21). It is observed that  $AMB-AMN$ , the resultant angular momentum supply, agrees nicely with the time derivative of the angular momentum,  $d(AM)/dt^*$ .

The results shown in Figs.33 and 35 suggest that the size of the backflow is determined by different mechanisms for quasi-steady and unsteady cases. For the quasi-steady case, the size of the backflow is determined from the supply of the angular momentum by the backflow,  $AMB$ , and the outflow of the angular momentum on the normal flow,  $AMN$ . For the case with a flow rate fluctuation, the difference ( $AMB-AMN$ ) contributes to the growth of the angular momentum in the upstream,  $d(AM)/dt^*$ .

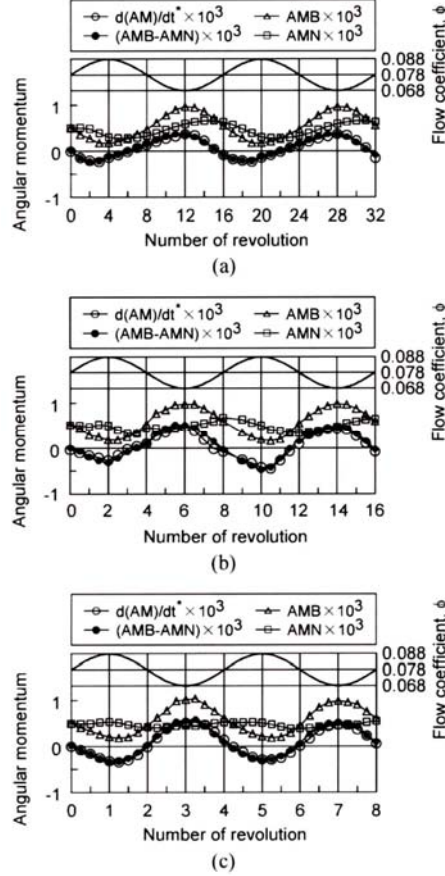


**Fig. 35** Conservation of angular momentum, (a)  $f/f_n=0.0625$ , (b)  $f/f_n=0.125$ , (c)  $f/f_n=0.25$

### 3.3 Mechanism of Backflow and Quasi-steady Response of $AMB$

In Fig.33, it was shown that the angular momentum supplied by the backflow,  $AMB$ , depends only on the instantaneous flow rate, with minor effects of unsteadiness. To examine the mechanisms of the backflow, Fig.36(a) shows the region with negative axial velocity in the cross section including the leading edge at the tip. The region with negative velocity is limited to the proximity of the casing, and the region ahead of the leading edge near the tip. Figure 36(b) shows the velocity field in the meridional plane shown in Fig.36(a). The flow is coming out from the pressure side of the leading edge. Similar results are obtained for the case without tip clearance [11]. These results suggest that the backflow comes mainly from the clearance between the swept part of the leading edge and the casing, driven by the centrifugal force and the pressure difference across the blade near the leading edge.

Figure 37 shows the instantaneous pressure distribution near the tip of blade (at  $r/R_t=0.99$ ) for the case with  $f/f_n=0.25$ , along with the quasi-steady pressure distribution. The results are shown for three instants when the flow rate becomes  $\phi=0.068$  (minimum),  $0.078$  (mean), and  $0.088$  (maximum). For  $\phi=0.078$ , the effect of inertia is canceled out by taking the average of the results in the increasing and decreasing phase of  $\phi$ . It is found that the instantaneous pressure distribution is nearly identical to the quasi-steady distribution.

These two facts that the backflow is driven by the centrifugal force and the pressure difference across the blade, and that the pressure distribution is quasi-steady explain why the angular momentum supplied by the backflow,  $AMB$ , depends only on the instantaneous flow rate, with minor effects of unsteadiness.



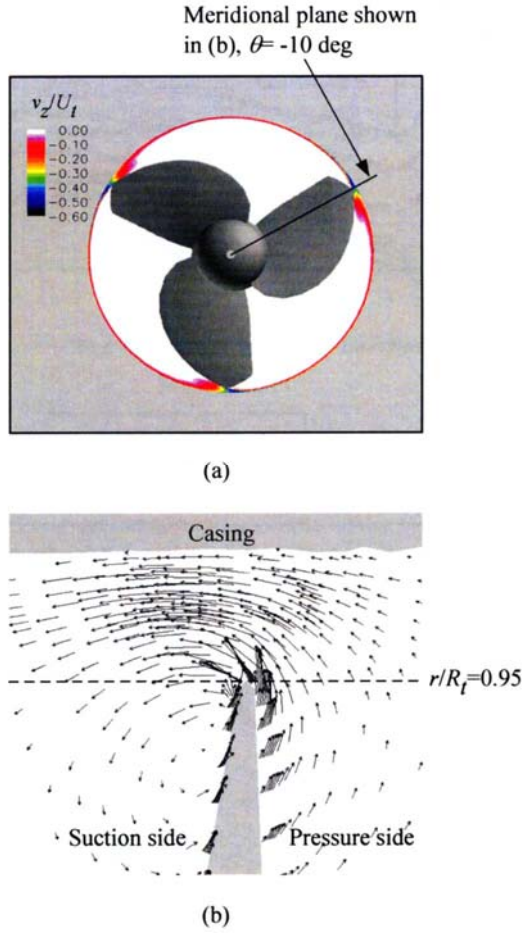


**Fig. 36** (a) Region with negative axial velocity and (b) velocity field in meridional plane

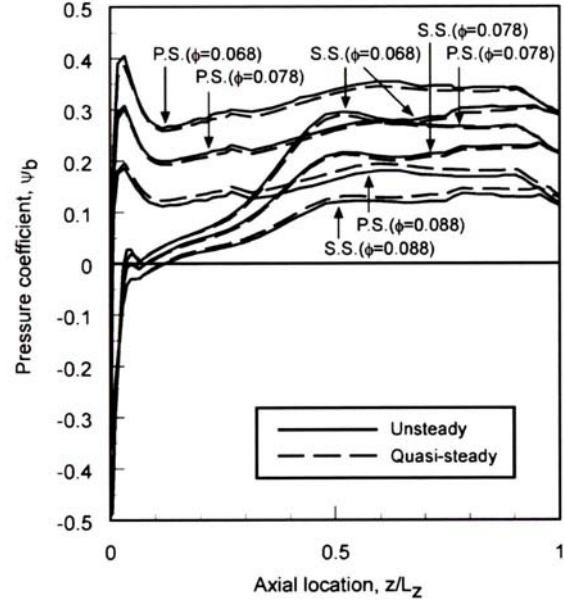


**Fig. 37** Comparison of steady and unsteady pressure distributions on the blade

### 3.4 Response Function of Backflow

To examine the phase relationship more quantitatively, the quantities are separated into mean (denoted by an overbar) and fluctuating (denoted by a tilde) components:

$$AM = \bar{A} + \tilde{A} \exp(j\omega^* t^*), \quad AMB = \bar{B} + \tilde{B} \exp(j\omega^* t^*), \quad AMN = \bar{N} + \tilde{N} \exp(j\omega^* t^*), \quad \phi = \bar{\phi} + \tilde{\phi} \exp(j\omega^* t^*)$$

where  $\omega^* = \omega(D_t/U_t) = 2(f/f_n)$  is a non-dimensional frequency.

Since the angular momentum supplied by the backflow is increased when the flow rate is decreased, we can express

$$\tilde{B} = -a\tilde{\phi} \quad (22)$$

The angular momentum removal by the normal flow would be larger if the angular momentum in the upstream and the flow rate is larger. So, we can assume

$$\tilde{N} = b\tilde{A} + c\tilde{\phi} \quad (23)$$

where,  $a$ ,  $b$ , and  $c$  are real constants. By putting these expressions into the angular momentum conservation equation (21), we obtain the response function

$$\frac{\tilde{A}}{\tilde{\phi}} = -\frac{a+c}{b+2j(f/f_n)} \quad (24)$$

This clearly shows that the angular momentum of backflow responds to the flow rate fluctuation as a *first order lag element*. For the case with  $f/f_n \rightarrow \infty$ , the phase of angular momentum in the upstream advances by 90deg ahead of flow rate fluctuation and delays by 90deg behind the quasi-steady backflow response.

To determine the values of proportionality constants  $a$ ,  $b$ , and  $c$ , numerical results for  $AM$ ,  $AMB$ , and  $AMN$  are Fourier-analyzed over two periods and the values of  $\tilde{A}$ ,  $\tilde{B}$  and  $\tilde{N}$  are determined from the first order components. The value of  $a$  is determined by neglecting the small phase difference between  $\tilde{B}$  and  $\tilde{\phi}$ . The values of  $b$  and  $c$  are determined from the real and imaginary parts of Eq.(23). The values of constants determined from the numerical results with  $f/f_n = 0.0625, 0.125$  and  $0.25$  are shown in Table 2. The value of parameter  $c$  is smaller as compared with others.

By putting the averaged values of  $a$ ,  $b$ , and  $c$  shown in Table 2 into Eq.(24), the complex representation of the response function  $\tilde{A}/\tilde{\phi}$  is obtained and shown in Fig.38. The values of  $\tilde{A}/\tilde{\phi}$  for  $f/f_n = 0.0625, 0.125$  and  $0.25$  determined from the numerical results are also shown in the figure. The data points of numerical results are close to the response function suggesting

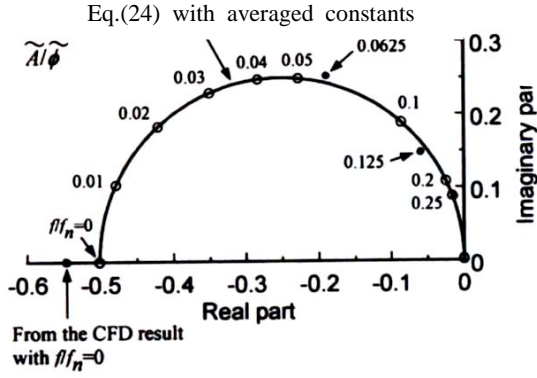


**Table 2** Values of parameters in the response function of Eq.(24)

	<i>a</i>	<i>b</i>	<i>c</i>
$f/f_n=0.0625$	0.0397	0.0930	0.0095
$f/f_n=0.125$	0.0411	0.1020	0.0020
$f/f_n=0.25$	0.0428	0.0783	0.0020
Averaged values	0.0412	0.0911	0.0045

**Fig. 38** Response function of backflow, Eq.(24), with the averaged values of parameters shown in Table 2

that the approximations of Eqs.(22) and (23) used for the derivation of the response function (24) are adequate. This response function clearly shows how the magnitude  $|\tilde{A}/\tilde{\phi}|$  decreases and the phase delays as we increase the frequency  $f/f_n$ . It also shows that the frequency of  $f/f_n=0.125$  is sufficiently large to cause the large delay behind the quasi-steady response.

We now return to the experimental result shown in Fig.30. Since the rotational speed is 3,000rpm or 50Hz, 5Hz corresponds to  $f/f_n=0.1$ . This shows that the phase delay observed in the experiment is somewhat larger. This is perhaps because the inlet velocity measurements were used in the experiment, for which the direct effect of flow rate fluctuation is overlapped. The phase delay larger than 90 deg observed with  $l_m/D_i=2.29$  might be caused by the fact that the amplitude of backflow response becomes smaller at higher frequency, as suggested by the result in Fig.39, and the backflow does not reach the measurement point.

The results presented above are based on CFD with a k-ε turbulence model which cannot simulate the vortex structure. However, recent studies based on LES show that the results are the same at least qualitatively even with the vortex structure.

## 4. Conclusion

- [1] For inducers, a backflow vortex structure appears even at design flow rate, as a result of the roll up of shear layer between swirling backflow and axial main flow.
- [2] As the flow rate decreases, the backflow vortex extends more upstream and moves to inner radial locations. The number of vortices gets smaller as the radial location of the vortices moves inward. This can be explained by a 2-D stability analysis.
- [3] The frequency of cavitation surge scaled with the inverse of the square root of the inlet pipe length but the effect of downstream pipe length was small, caused by larger resistance and inertance of the downstream hydraulic system.
- [4] With the cavitation surge occurring at smaller flow rates, the displacement work by cavitation was the major source of energy supply at higher cavitation number, while the contribution of pump work was larger at smaller cavitation number.
- [5] The cavitation compliance and mass flow gain factor was evaluated from the resonant frequency, assuming quasi-steady response of cavities. The value of mass flow gain factor obtained was positive and could not explain the cavitation surge observed.
- [6] Response of backflow was evaluated from the velocity measurement at the pump inlet. It was found that the phase delay approaches about 90deg when the frequency increases to about 10% of the rotational frequency. This frequency is called critical frequency. Below this frequency, the backflow cavitation will destabilize the hydraulic system.
- [7] The cavitation surge at low flow rate occurred when the resonant frequency becomes smaller than the critical frequency as the cavitation number is decreased.
- [8] Response of backflow to flow rate fluctuation was discussed from the balance of angular momentum at the inlet.
- [9] The angular momentum transfer by the backflow was in anti-phase with the flow rate fluctuation.
- [10] The angular momentum transfer by the normal flow was larger when the angular momentum in the upstream is larger.
- [11] From the balance of angular momentum, it was shown that the backflow responds to the flow rate fluctuation as a first order lag element.
- [12] Summary: Backflow vortex cavitation destabilizes low frequency oscillations from its quasi-steady characteristics but the destabilizing effect gets smaller as the frequency of oscillation is increased, due to the delay of response to flow rate fluctuation. Thus, the unsteadiness of cavity response including the flow process is important for the cases with backflow vortex cavitation.

## Nomenclature

<i>AM</i>	Angular momentum	<i>AMB</i>	Angular momentum transfer by backflow
<i>AMN</i>	Angular momentum transfer by normal flow	<i>A</i>	Aross-sectional area of pipe
$\tilde{A}$	Angular momentum fluctuation	<i>C<sub>p</sub></i>	Cavitation complianceFluid Density
<i>D, D<sub>i</sub></i>	Diameter	<i>E<sub>cl</sub></i>	Displacement work of cavitation
<i>E<sub>p1</sub></i>	Energy supplied by pump	<i>E<sub>vl</sub></i>	Energy dissipated by valve
<i>f</i>	Frequency	<i>f<sub>0</sub></i>	Resonant frequency
<i>g</i>	Gravitational acceleration constant	<i>H<sub>sv</sub></i>	Available suction head

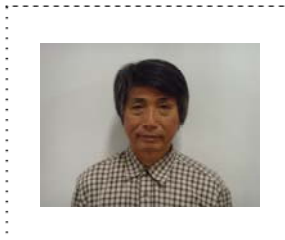
$j$	Imaginary unit	$K$	Cavitation number, $=H_{sv}/(U_I^2/2g)$
$M_b$	Mass flow gain factor	$P$	Pressure
$p$	Unsteady component of pressure	$Q$	Flow rate
$q$	Unsteady component of flow rate	$r$	Radius
$t, t^*$	Time, non-dimensional time	$U_b, U_t$	Tip velocity at inlet
$L$	Inertance, $=\rho l/A$	$l$	Length of pipe
$R$	Resistance	$V_c$	Cavity volume
$z$	Axial coordinate	$\gamma$	Specific weight
$\rho$	Density of fluid	$\phi$	Flow coefficient
$\psi$	Pressure coefficient	$\sigma$	Cavitation number based on static pressure

## References

- [1] Yokota, K., Kuwahara, K., Kataoka, D., Tsujimoto, Y., and Acosta, A., 1999, A Study of Swirling Backflow and Vortex Structure at the Inlet of an Inducer, JSME International Journal, Ser.B, Vol.42, No.3, pp. 451-459.
- [2] Yokota, K., Mitsuda, K., Tsujimoto, Y., and Kato, C., "A Study of Vortex Structure in the Shear Layer between Main Flow and Swirling Backflow, 2004, JSME International Journal, Ser. B., Vol.47, No.3, pp. 541-548.
- [3] Milne-Thomson, Theoretical Hydrodynamics, 5th Ed., Macmillan & Co Ltd.
- [4] Yamamoto, K., 1990, Instability in a Cavitating Centrifugal Pump (1st Report, Classification of Instability Phenomena & Vibration Characteristics), Trans. JSME (in Japanese), Ser.B, Vol.56, No.523, pp. 82-89.
- [5] Yamamoto, K., 1990, Instability in a Cavitating Centrifugal Pump (2nd Report, Delivery of Mechanical Energy during Oscillation), Trans. JSME (in Japanese), Ser.B, Vol.56, No.523, pp. 90-96.
- [6] Yamamoto, K., 1990, Instability in a Cavitating Centrifugal Pump (3rd Report, Mechanism of Low-Cycle System Oscillation), Trans. JSME (in Japanese), Ser.B, Vol.58, No.545, pp. 180-186.
- [7] Tsujimoto, Y., Kamijo, K., and Brennen, C.E., 2001, Unified Treatment of Instabilities in Turbomachines, AIAA Journal of Propulsion and Power, Vol.17, No.3, pp. 636-643.
- [8] Brennen, C.E., and Acosta, A.J., 1976, The Dynamic Transfer Function for a Cavitating Inducer, ASME Journal of Fluids Engineering, Vol.78, No.2, pp. 182-191.
- [9] Qiao, X., Horiguchi, H., and Tsujimoto, Y., 2007, Response of Backflow to Flow Rate Fluctuations, ASME Journal of Fluids Engineering, Vol.129, No.1, pp. 350-357.
- [10] Yamanishi, N., Fukao, S., Qiao, X., Kato, C., and Tsujimoto, Y., 2007, LES Simulation of Backflow Vortex Structure at the Inlet of an Inducer, ASME Journal of Fluids Engineering, Vol.129, No. 2, pp. 587-594.
- [11] Qiao, X., Horiguchi, H., Kato, C., and Tsujimoto, Y., 2001, Numerical Study of Backflow at the Inlet of Inducers, Proceedings of the 3rd Int. Symp. On Fluid Machinery and Fluid Engineering, Beijing, China, A-1, pp. 1-11.



**Kazuyoshi Yamamoto** B.E.(1967), M.E.(1970), Dr.Eng.(1992) from Yokohama National University  
Ishikawajima Harima Heavy Industry (1967), Ebara Corporation (1970), Ebara Research Corporation(1984), Director General Manager of Center for Technology Development of Ebara Research Corporation(1998), Managing Director of Ebara Research Corporation(2000), Technical Super-intendant of Ebara Corporation(2002), Professor of Japan Advanced Institute of Science and Technology, Director of Center for Research and Investigation of Advanced Science and Technology(2003- ).



**Yoshinobu Tsujimoto** B.E.(1971), M.E.(1973), Dr.Eng(1977) from Osaka University, Research Associate of Engineering Science, Osaka University (1977), Associate Professor of Engineering Science, Osaka University (1986), Professor of Engineering Science, Osaka University (1989-).